Influence of the Molar Ratio of Co and V in Bimetallic Oxides on Their Pseudocapacitive Properties

Lady V. Quispe-Garrido, Ivonne E. Monje, Elvis O. López, Josué M. Gonçalves, Cleonice S. Martins, Gabriel Ángel Planes, José G. Ruiz-Montoya, and Angélica Maria Baena-Moncada*

Cite This: *ACS Omega* 2022, 7, 43522−43530

Read Online

ACCESS | 📊 Metrics & More | 📖 Article Recommendations | 🔵 Supporting Information

ABSTRACT: Bimetallic oxides have significant attraction as supercapacitor electrode materials due to their highly reversible redox processes, which are commonly associated with their surface chemistry and morphological features. Here, we report the synthesis, characterization, and electrochemical evaluation of bimetallic oxides with different molar compositions of Co and V ($Co_{0.6}V_{0.4}$, $Co_{0.64}V_{0.36}$, $Co_{0.68}V_{0.32}$, and $Co_{0.7}V_{0.3}$ denoted as S1, S2, S3, and S4 samples, respectively). The materials were synthesized by a modified solvothermal method using glycerol as a stabilizing agent, characterized by X-ray diffraction, Raman spectroscopy, X-ray photoelectron spectroscopy, transmission electron microscopy, scanning electron microscopy−energy-dispersive X-ray spectroscopy, X-ray fluorescence spectroscopy, N_2 adsorption isotherms, cyclic voltammetry, and galvanostatic charged/discharged in a three-electrode cell. The role of the CoV oxide compositions on the pseudocapacitive properties was studied through the analysis of the energy storage mechanism following the power law and Dunn's methodology to obtain the *b* values. An important finding of this work is that CoV oxides exhibited electrochemical characteristics of a pseudocapacitive electrode material even though the charge storage occurs in bulk. This behavior is consistent with the pseudocapacitance generated by redox processes, showing *b* values of 0.67, 0.53, 0.75, and 0.84, with a capacitive current contribution of 74, 74, 63, and 70% analyzed at a scan rate of 1 mV s^{-1}, for S4, S3, S2, and S1 samples, respectively. $Co_{0.7}V_{0.3}$ (S4) oxide presented the highest specific capacitance of 299 F g^{-1} at 0.5 A g^{-1} with a Coulombic efficiency of 93% tested at 4 A g^{-1}. The better electrochemical performance of this sample was attributed to the synergistic effect of the Co and V atoms since a minimum amount of V in the structure may distort the crystal lattice and improve the electrolyte diffusion, in addition to the formation of several oxidation states due to reduction of V^{5+}, including V^{3+} and V^{4+} as well as to the formation of the metastable V_4O_9.
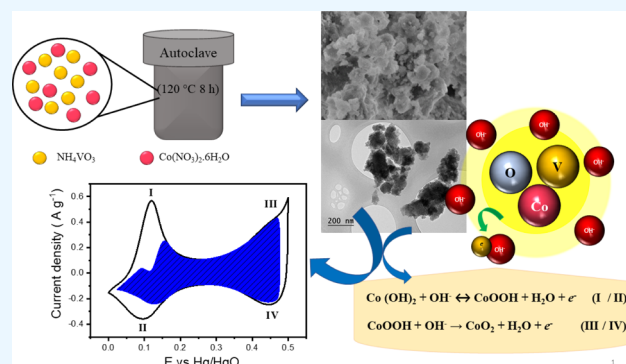
1. INTRODUCTION

In recent years, global warming concerns originating mostly because of the massive use of fossil fuels are driving the development of intermittent energy sources and hybrid electric vehicles. Consequently, efficient and economical energy storage systems are required.[1]

Electrochemical capacitors (ECs), also called supercapacitors, and rechargeable batteries are considered the most convincing electrochemical energy storage devices.[2] In particular, supercapacitors generally offer charge storage properties that complement those of batteries[3] and are of great interest in applications that require high power for a short time.[4] However, affordable cost and high energy density are still required to achieve wide market penetration.[5] Thus, lots of efforts are being made globally toward improving the charge and energy storage density by exploring new electrode materials since this aspect is one of the most critical components that defines the performance of an EC.

Supercapacitors are generally divided according to their capacitive behavior: electrochemical double-layer capacitors (EDLCs) and pseudocapacitors (PCs). The EDLC behavior consists of an electrode−electrolyte interface that depends on rapid and reversible ion adsorption/desorption to form the electrical double-layer capacitance.[6] For pseudocapacitive materials, the total stored charge can be conventionally separated into two parts, surface (or outer) and bulk (or inner) processes, in which the charging mechanism can be due to the following three forms: (i) monolayer adsorption of ions at an electrode surface, (ii) surface redox reaction, and (iii) ion

intercalations without phase change, in which the charge storage occurs in the bulk material.[7]

Binary transition metal oxides based on RuO_2 have been well studied due to their high theoretical specific capacity ($200-1200$ F g^{-1}).[8] However, despite the high specific capacitance (SC), the high cost of Ru-based materials is a serious disadvantage.[9] Consequently, alternative less costly and more abundant transition metal oxides have surged as interesting options.

Some strategies in the synthesis methodologies include increasing more electroactive sites to generate more Faradaic reactions and improve the electrochemical performance.[10,11] Bimetallic oxide compounds (e.g., Ni−Co, Mn−Co, Co−Ru, and Co−V),[12,13] trimetallic[14] or higher order metal oxides and core−shell structures of oxides,[15−17] are attractive since they can introduce structural defects, undergo additional fast redox reactions, and provide higher electrical conductivity compared to monometallic oxides.[18,19] Regarding CoV oxides, recently, several studies with interesting morphologies and capacitances have been reported, for instance, $Co_3V_2O_8$ nanoplates,[18] $Co_3V_2O_8$ porous rose-like structures,[20] $Co_2V_2O_7 \cdot 3H_2O$ micro-flowers,[21] CoV_2O_6 micron blocks,[22] and $Co_3V_2O_8$ nanoparticles.[22,23] All these mentioned bimetallic materials show morphological, structural, and compositional differences adopting different charge storage mechanisms. However, despite this observation, scarce information is available on the influence of compositional variation of Co and V on the storage mechanism and its capacitance, the latter is the aim of this article.

In this work, the influence of the Co and V composition at different concentrations with respect to the pseudocapacitive storage mechanisms and electrochemical signature was evaluated. The materials were synthesized using four different Co/V molar ratios from a modified solvothermal method reported by Zhang et al.[18] and glycerol as a stabilizing agent. The samples were characterized by X-ray diffraction (XRD), Raman spectroscopy, scanning electron microscopy (SEM), energy-dispersive X-ray spectroscopy (EDS), nitrogen gas adsorption isotherms, X-ray photoelectron spectroscopy (XPS), and X-ray fluorescence (XRF) spectroscopy. Further, composite electrodes were prepared with these CoV oxides and characterized by cyclic voltammetry (CV) and galvanostatic charge−discharge. Finally, we have analyzed (i) the pseudocapacitive properties of the CoV oxides through the values of b (between 0.5 and 1) obtained from the power law and (ii) the current contributions from diffusion-controlled and surface-controlled processes, respectively, obtained using Dunn's methodology. The results indicate that the electrochemical properties of the synthesized CoV oxides showed different capacitance influences for the Co/V composition.

2. METHODOLOGY

2.1. Materials. All the chemicals were of analytical grade and used without further purification: $Co(NO_3)_2 \cdot 6H_2O$ (99%, Merck), NH_4VO_3 (99%, Merck) (99%, Merck), NaOH (99%, Merck), glycerol (98%, Panreac Química S.A.), KOH (85%, Merck), Nafion (5 wt %, Merck), and EtOH (99.9%, Scharlau). In addition, Millipore water was used throughout all the experiments.

2.2. CoV Oxide Synthesis. For the synthesis of a typical CoV oxide, two flasks were labeled A and B. In flask A, NH_4VO_3 (62.9 mg, 0.54 mmol) was dissolved in 5 mL of water at 80 °C and vigorously stirred for 10 min. In container B,

$Co(NO_3)_2 \cdot 6H2O$ (234.9 mg, 0.81 mmol), 5 mL of glycerol, and 10 mL of ethanol were added and magnetically stirred at room temperature for 10 min; then, a NaOH solution was added drop by drop until a pH = 10 was reached. The C solution, obtained from the mixture of flasks A and B, was stirred for 15 min with pH in the range of 8−9. Then, the C solution was transferred into a 25 mL Teflon-lined stainless steel autoclave, followed by heating at 120 °C for 8 h. After cooling at room temperature, the solid product was washed with an H_2O/EtOH solution and dried at 100 °C for 3 h in a furnace; this oxide was denoted as S3. Similar experimental conditions to the above-mentioned procedure were followed for the rest of the CoV oxides. The synthesized materials did not undergo post-synthesis heat treatment to promote cost-effective conditions favorable for large-scale production. The nominal composition and nomenclature used in this paper are given in Table 1.

Table 1. Nominal Composition of Synthesized CoV Oxides[a]

sample	Co $(NO_3)_2 \cdot 6H2O$ (mmol)	NH_4VO_3 (mmol)	nominal Co/V ratio*
S1	0.47	0.93	0.33:0.67
S2	0.68	0.68	0.50:0.50
S3	0.81	0.54	0.60:0.40
S4	0.89	0.44	0.67:0.33

[a]The nominal Co/V ratio is calculated for Co_xV_y ($x + y = 1$).

2.3. Physicochemical Characterization. The crystalline structure of the powders was investigated using a PANalytical Empyrean X-ray diffractometer with a PIXcel 3D detector. Data were collected using a Cu Kα radiation at 40 kV and 40 mA of energy, with the 2θ detector varying between 20 and 70° in steps of 0.026° and an integration time of 600 s per step.

The morphological and elemental compositions were analyzed using a high-resolution scanning electron microscope from a field emission gun (FEG-SEM) of JEOL company (model JSM-7100F), equipped with an EDS detector. The measurements were carried out at a 15 kV of energy, a work distance of 8 mm, and in different amplifications. Transmission electron microscopy (TEM) images were obtained using JEM-2100 equipment (JEOL) at an acceleration voltage of 200 kV . For this, 5 μL of the suspension in water/ethanol (1:1 vol/vol) was deposited onto an ultrathin carbon film-coated copper grid (Ted Pella Inc.).

Raman spectra were obtained in backscattering geometry at room temperature using a home-built Raman spectrometer equipped with an Andor Shamrock spectrometer with an iDus charge-coupled device detector, a laser of 488 nm (~2.54 eV), and a home-made optical system. All measurements were obtained using a laser spot size of 1 μm at a power of 400 μW. The spectral resolution was adjusted from the full width at half-maximum of a silicon wafer (520 cm^{-1}) at 4 cm^{-1}.

The surface chemical composition was analyzed by XPS measurements using the SPECS PHOIBOS 100/150 spectrometer with a hemispheric analyzer operating at 1486.6 eV of Al Kα1. The spectra were collected with a high-resolution monochromatic X-ray source within an energy step of 0.02 eV. A processing software (CasaXPS, SPECS Software) was used to adjust the envelope peaks of Co 2p, V 2p, O 1s, and C 1s levels to determine the chemical binding energies (BEs) of some formed species, as well as to calculate the relative atomic quantities on the samples. The difference in the 2p spin−orbit

levels for Co and V was calculated as $\Delta Co(2p_{1/2} - 2p_{3/2}) =$ 16.0 eV and $\Delta V(2p_{1/2} - 2p_{3/2}) = 7.4{-}7.9$ eV. The spectra were calibrated by using the hydrocarbon at C 1s = 284.6 eV.

XRF analyses were carried out using a Panalytical, Axios mAX model at a power of 3.0 kW to calculate the metal composition in the samples. The results were obtained through the semiquantitative analysis using the Ominan program. The calibration curves use standard samples manufactured by the Panalytical Company. To carry out the measurements, it was necessary to prepare a tablet using 0.03 g of sample and 7.0 g of fondant. A flow of tetraborate and lithium metaborate in the proportion of 66/34 at 1200 °C was used to melt the samples. Specific surface areas were performed using the Brunauer–Emmett–Teller (BET) method using a Micromeritics ASAP 2020 Plus equipment with an initial vacuum condition of 1.33 Pa, and nitrogen gas as an adsorptive element was used to perform the measurement. The samples were degassed under vacuum at 6.66 Pa, then heated at 1.0 °C min^{-1} to reach 100 °C, and kept for 360 min at the same residual pressure.

2.4. Electrode Preparation and Electrochemical Characterization. The samples' electrochemical performances were measured in a three-electrode cell in a 1 mol L^{-1} KOH aqueous solution as an electrolyte. CoV oxide electrode materials (2 mg) (previously milled in agate mortar) and 15 μL of Nafion 5 wt % were dispersed in 500 μL of water and sonicated for 30 min to form a homogeneous ink. Subsequently, 10 μL of the ink was coated onto a glassy carbon electrode of 3 mm diameter to form the working electrode. A Pt wire and a Hg/HgO (1 mol L^{-1} KOH) electrode were used as a counter electrode and reference electrode, respectively. Cyclic voltammograms and GCD curves were measured by an Autolab PGSTAT302N (Metrohm) potentiostat/galvanostat analyzer. The specific capacitance (Cs) can be calculated according to eq 1

$$Cs = \frac{I \times t_d}{(m \times \Delta V)} \tag{1}$$

wherein I (A), t (s), m (g), and V (V) represent the discharge current, discharge time, mass of active materials, and window potential, respectively.

The relationship between scan rate and anodic peak current (I_p) was analyzed to investigate the charge storage mechanism of CoV oxides with different Co/V molar ratios using the well-known power law expressed as

$$I_p = a\nu^b \tag{2}$$

$$\log I_p = \log a + b \log \nu \tag{3}$$

where a and b are adjustable variables; $b = 1$ indicates that the charge storage mechanism is surface-controlled, while $b = 0.5$ indicates that it is diffusion-controlled.[24]

3. RESULTS

3.1. Microstructural and Composition Analysis. Figures S1 (see the Supporting Information) displays the SEM images of S1, S2, S3, and S4 and TEM images of S1 and S4 samples. These micrographs indicate that all samples consist of agglomerated irregularly shaped particles with a particle size of a few microns but without significant morphology differences. Table 2 shows the XRF results for all samples, the average local compositions observed by EDS (Figure S2 provides evidence of a uniform distribution of

Table 2. Co/V Atomic Ratio in the Bulk, Specific Surface Area, and Particle Size Were Obtained from the Scherrer Equation

sample	EDS (Co/V)^a	fluorescence (Co/V)^a	specific surface area (m^2 g^{-1})^b	crystallite size of (221) plane, (nm)^c
S1	0.52:0.48–0.57:0.43	0.60:0.40	2.1	4.5
S2	0.58:0.42–0.64:0.36	0.64:0.36	2.9	3.8
S3	0.63:0.37–0.68:0.32	0.68:0.32	6.0	4.2
S4	0.68:0.32–0.71:0.29	0.72:0.28	6.2	3.4

^{a}From EDS and XRF data. ^{b}From BET analysis. ^{c}From XRD data.

elements in sample S4), as well as the specific surface area from BET analysis (see N$_2$ adsorption isotherms in Figure S3) and particle sizes obtained from the Scherrer equation from the XRD data shown in Figure 1a.
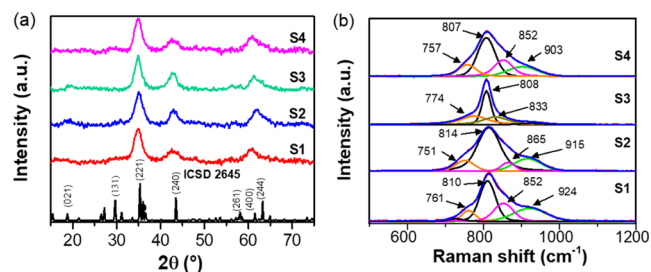

Figure 1. Structural characterization of the CoV oxide samples measured by XRD (a) and Raman spectroscopy (b).

The XRD patterns for all samples (Figure 1a) display a single phase of Co$_3$V$_2$O$_8$ with an orthorhombic structure, space group of *Cmca* (ICSD 2645).[25] The peaks' broadening show a microstructural disorder in these samples produced by the adsorption of structural water in the materials,[26] which is because the samples were not calcined. The crystallite size of these samples, obtained by the Scherrer method, varied between 3.4 and 4.5 nm as shown in Table 2. No other diffracted angles were observed in the samples.

Raman spectra fitting of all samples is shown in Figure 1b. Bands around 810 cm^{-1} were associated with the symmetric vibration V–O and the asymmetric stretching V–O–Co bonds.[27] The narrowing of 808 cm^{-1} band position in the S3 sample is related to a good structural organization. Bands between 900 and 930 cm^{-1} are due to the vibrations of the V^{4+}=O bonds,[28,29] while bands at 850 cm^{-1} can be associated with V=O stretching promoted by a structural disorder.[30] The band at around 760 cm^{-1} was observed in metastable formations of V$_4$O$_9$ (V$^{4.5+}$ oxidation state);[30] this is reinforced by a vibration at 906 cm^{-1}, which is presented in the S4 sample. Furthermore, the formation of this metastable phase is due to the reduction processes starting from V^{5+}.[31]

The XPS results for all samples are shown in Figure S4 and Table S1, where the formation of oxides and hydroxides on the samples surface is confirmed. Figure 2a,b shows the high-energy resolution of Co 2p and V 2p (V 2p together with O 1s) levels for S1 and S4 samples. The BE of Co 2p$_{3/2}$ was 782.2 eV and 781.4 eV for S1 and S4 samples, respectively, both correspond to the oxidation states of Co^{2+}, forming Co(OH)$_2$ bonds.[32–34] Satellite peaks were also observed in Co 2p$_{3/2}$ with energies around 786.8 ± 0.3 eV. Three different oxidation states were observed at the V 2p$_{3/2}$ level, for both samples. In
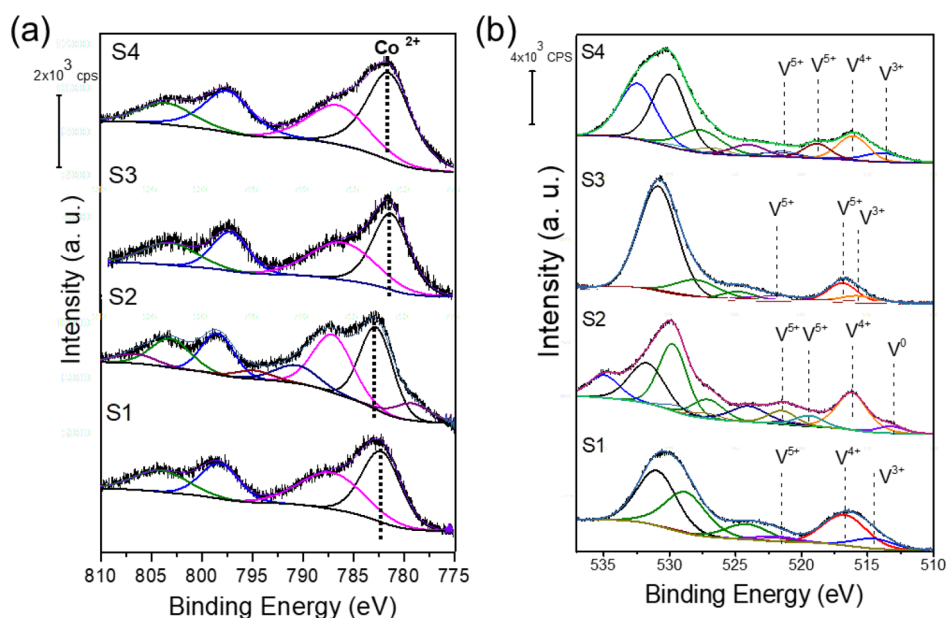
Figure 2. XPS spectra of the Co 2p (a) and V 2p (V 2p together with O 1s) levels of the S1, S2, S3, and S4 samples (b).

the S1 sample, the BE of V $2p_{3/2}$ was observed at 514.5 and 516.7 eV, which correspond to the oxidation states of V^{3+} and V^{4+}, respectively.[32,35] In addition, a higher BE was observed at 521.8 eV, which corresponds to V^{5+} formed by a metal-to-ligand complex through electron transfer.[36] In S4, the BE of V $2p_{3/2}$ at 513.9 and 516.1 eV represents the oxidation states of V^{3+} and V^{4+} forming well-defined $V(OH)_3$ and V_2O_4 species, respectively.[35,37] Besides, an increase in vanadium concentration is also observed at a BE of 521.5 eV, as well as the formation of V_2O_5 species (V $2p_{3/2}$ = 518.8 eV) produced by an oxidation−reduction process.[38]

3.2. Electrochemical Property Evaluation. The electrochemical properties of the four CoV oxide electrodes were initially characterized by CV, and the results are shown in Figure 3. Figure 3a shows the cyclic voltammograms obtained
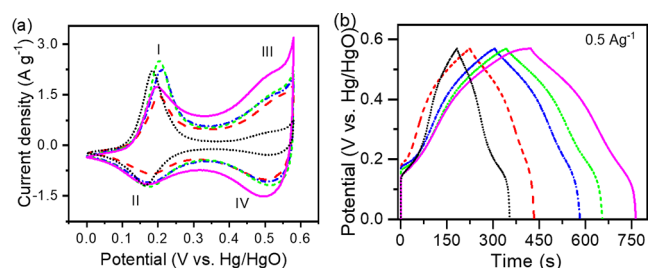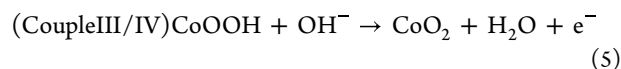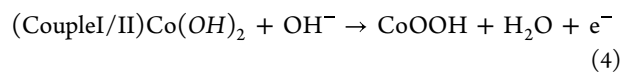

Figure 3. CV curves of the synthesized CoV oxides at a scan rate of 5 mV s^{-1} in 1 mol L^{-1} KOH (a) and GCD at 0.5 A g^{-1} in the range from 0.0 to 0.57 V (b). S1 (red em dash), S2 (blue em dash), S3 (green em dash), and S4 (pink em dash) and CoO$_x$ (black circle solid).

in the potential range from 0 to 0.58 V *versus* Hg/HgO at 5 mV s^{-1} in 1 mol L^{-1} KOH as an electrolyte. Note that pure CoO$_x$ has also been included for comparison. The shape of the CV curves provides evidence of two anodic peaks during the forward scan, situated at 0.2 and 0.5 V, and corresponding to Co-oxidation Co^{2+}/Co^{3+} (0.2 V, assigned as I) and Co^{3+}/Co^{4+} (0.5 V, assigned as III). During the Faradaic reduction processes, two complementary anodic contribution peaks are

clearly visible at 0.5 and 0.17 V according to Co^{4+}/Co^{3+} and Co^{3+}/Co^{2+} transition (denoted as IV and II, respectively). Both couples of peaks are in agreement with previous reports[7,39] and could be associated with the following reversible reactions

$$(\text{Couple I/II}) \, Co(OH)_2 + OH^- \rightarrow CoOOH + H_2O + e^- \tag{4}$$

$$(\text{Couple III/IV}) \, CoOOH + OH^- \rightarrow CoO_2 + H_2O + e^- \tag{5}$$

Complementary and valuable information about the electrochemical behavior of the electrode is obtained from GCD analysis. The charge storage abilities of the as-prepared oxide materials were determined in the first instance in a constant current density of 0.5 A g^{-1}, as shown in Figure 3b. In good agreement with the CV curves (Figure 3a), the symmetric shape of the charge/discharge curve, with the existence of small plateaus taking place at the same potential during both charging and discharging processes, display a well reversible behavior up to 0.57 V for all analyzed samples. As has been previously mentioned for CV curves, all electrodes that have been tested show reversible contribution of reaction (eq 4), visible in the GCD curves as a small plateau at 0.15−0.25 V, while the plateau at 0.45−0.55 V corresponds to eq 5. It is important to mention that for potentials as high as 0.55 V, the oxygen evolution reaction (OER) parasitism limits the increase of the potential window in lower current densities,[40] as observed by the increase in the oxidation current (Figure 3a) and the presence of a plateau in the GCD curves (Figure 3a), especially for sample S4.

Additional information about the SC, rate capability, and Coulombic efficiency for each sample has been shown in Figure 4a−d. The highest capacitance value observed at 0.5 A g^{-1} (Figure 4a) corresponds to the Co-rich sample (S4, 299 F g^{-1}), which was twice the capacitance of the V-free CoO$_x$ (150 F g^{-1}). A comparison of the rate performance measured at current densities of 6, 4, 2, 1, and 0.5 A g^{-1}, respectively, is gathered for all samples and displayed in Figure 4b. Independent of the current density applied, the best perform-
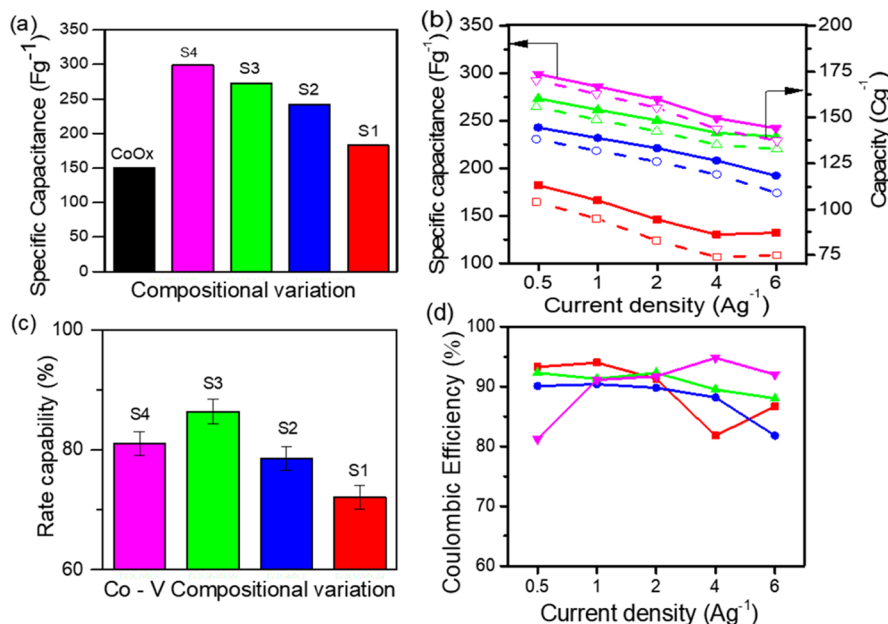
Figure 4. Bar diagram of the SC calculated from figure 4b (a); SC (continuous line) and capacity (dashed line) as a function of the current density (b); rate capability or specific capacity retention as a function of the Co−V molar ratio (c); and Coulombic efficiency of S4 (▼), S3 (▲), S2 (●), and S1 (■) (d).

ance in terms of SC is always achieved by sample S4. However, in terms of rate capability (Figure 4c), sample S3 shows the lowest capacity drop (about 13%), slightly below the sample S4 (20%), which results in a rate capability of 87 and 80%, respectively. The smaller capacity decrease of S3 sample may be associated with good structural organization, as evidenced by Raman analysis (see Figure 1b). Electrochemical impedance (EIS) analysis was performed to evaluate the conductivity of samples S1, S2, S3, and S4, where the results showed S1 > S2 > S4 > S3 (see Figure S5). However, S3 and S4 presented the highest SCs and better rate capabilities compared to S1 and S2 (see Figure 4a,c).

The Coulombic efficiency (η) (Figure 4d) is an analysis of the reversibility of ion insertion and de-insertion that take place during the charge/discharge processes. It was calculated for each charge/discharge cycle using the equation $\eta = t_d/t_c \times 100$, where t_c and t_d represent the charging and discharging time, respectively. All samples show a Coulombic efficiency above 80%, with a maximum value of 93% for sample S4 when it was tested at 4 A g^{-1}.

The b values were analyzed at different scan rates of 0.5, 1, 2, 5, and 10 mV s^{-1} to investigate the charge storage mechanism of CoV oxides with different Co/V molar ratios (see Figure S6), and the results are summarized in Figure 5a. Most CoV oxides show low b-values in the range from 0.1 to 0.15 V, previous to the first oxidation peak (I). Once the Co(OH)$_2$ conversion to CoOOH takes place ($E > 0.15$ V), the b-values sharply increase to 1. Figure 5b shows typical b-value analysis exemplified for $E = 0.125$ V. The obtained b-values at $E = 0.125$ V were 0.67, 0.53, 0.75, and 0.84 for S4, S3, S2, and S1, respectively.

In addition, using the concepts presented above, we can express the current response at a fixed potential as being the combination of two separate mechanisms, surface- and diffusion-controlled processes[41] as shown in eqs 6 and 7
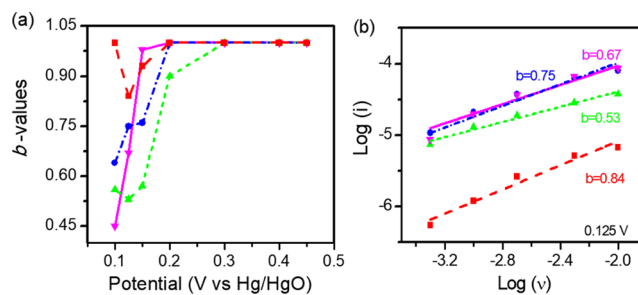
$$i_V = k_c \nu + k_d \nu^{1/2} \tag{6}$$

Figure 5. b-values as a function of potential (a) and power law dependence on current at scan rate, following the eq 6, evaluated at 0.125 V (region I from Figure 3a) for (b) S4 (▼), S3 (▲), S2 (●), and S1 (red box solid) samples.

$$\frac{i_V}{\nu^{1/2}} = k_c \nu^{1/2} + k_d \tag{7}$$

where k_c and k_d correspond to the current contributions from the surface capacitive effects (pseudocapacitance) and the diffusion-controlled intercalation process (battery-like), respectively. Thus, by determining k_c and k_d, we are able to quantify, at specific potentials, the fraction of the current due to each of these contributions (see Tables S2 and S3).

Figure 6a shows the contribution percentages for surface-controlled currents (shaded areas); these values were 72, 74, 63, and 70 for S1, S2, S3, and S4 samples (Figure 6b) and 58% for CoO$_x$ (see Figure S7). It is worth mentioning that this analysis was performed at 1 mV s^{-1}, and the scan rate was lower than the analysis studied in Figure 3a, resulting in a displacement of the potentials in all redox processes.

On the other hand, the analysis of the contributions of capacitive and diffusion currents at 0.5 and 10 mV s^{-1}, respectively, clearly shows that the capacitive contribution has increased markedly with increasing scan rate (see Figure S8). In fact, even at a slow scan rate of 0.5 mV s^{-1}, the percentage of total charge resulted from surface-controlled capacitive
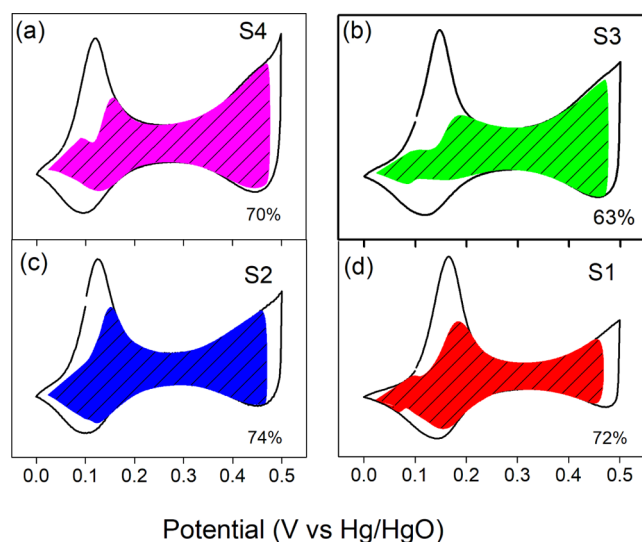
Figure 6. Voltammetric response at 1 mV s^{-1} from the four oxides S4 (a), S3 (b), S2 (c), and S1 (d); the total current (solid line) was obtained experimentally. The capacitive currents (shaded regions) were determined using the eq 5.

processes is greater than 55% for all samples (see Figure S8), which could be attributed to an amorphous structural disorder and interconnected particles produced on the surface of the oxides during synthesis.[42] In addition, the excellent pseudoca-pacitive charge storage with a fast charge/discharge process could be attributed to highly reversible redox reactions, shorter ion diffusion lengths, and continuous access to electroactive sites.[43] Therefore, the storage mechanism in Co−V oxide materials is Faradaic in nature with a considerable pseudocapacitive behavior.

4. DISCUSSION

According to the above analysis, these results suggest that the synthesis conditions explored here can be tailored to obtain CoV oxide nanomaterials with different molar ratios. In addition, this procedure also enables to obtain CoV oxides with low production cost owing to the simplicity of the process (120 °C as the synthesis temperature and absence of heat treatment) as well as using cheap glycerol as a stabilizing agent. The synthesis of CoV oxide was performed using different molar composition ratios according to Table 1. However, high differences in the obtained composition after the synthesis are observed in XRF and EDS results; those differences are probably due to the elimination of segregates and small particles during sample washing.

Results obtained by Raman and XPS suggest that all sample surfaces are rich in vanadium. Besides the observation that the formation of metastable phases ($V^{4.5+}$) obtained from the V^{5+} reduction, these phases can contribute to the release and capture of electrons when applied to different potentials. In addition, Raman spectroscopy and XPS reveal different oxidation states in all the samples that can be responsible for the enhancement of the electrochemical properties.

From this result, it can be inferred that the synthesized materials are composed of nanostructures with defined crystalline phases but also covered by low-order crystalline or amorphous materials constituted by Co and V (not identified by XRD directly), where the latter are responsible for forming the hydrated elements also observed by XPS (see Table S1).

Unfortunately, high-resolution TEM measurements were not obtained to confirm this hypothesis, but XRD, Raman, and XPS measurements indicate this hypothesis.

On the other hand, a fast inspection of Figure 3a reveals the effect of V in the CoO$_x$ structure. While the charge involved in the peak I/III remains unaltered, the current in the range 0.25−0.55 V increases up to around 6 times when it is compared with V-free CoO$_x$. This fact suggests that while the total redox charge due to Co load remains unchanged, the Co(OH)$_2$ → CoOOH conversion in the presence of V produces a notorious increase in the electrochemically accessible structure. In addition, no substantial differences between the anodic (I) and cathodic peaks (II) are observed, which indicates good reversibility of the electrochemical reaction.[44,45] It is also observed that S4 shows a higher capacitive current in the potentials around 0.3−0.55 V, probably influenced by $V^{4.5+}$ formation and the crystalline lattice distortion in the presence of V. This hypothesis is also supported by the slightly shifted diffraction plane at 64° (see Figure 1a). Similar effects were observed for vanadium-doped nickel−cobalt layered double-hydroxide nanosheets, where vanadium contributes to increase the specific surface area and enhance the electrochemical reaction kinetics.[46] Furthermore, it has been previously reported that the insertion of V ions and a high amount of Co atoms provides the generation of CoOOH species. This CoOOH is recognized as a high conductor compound often associated with higher values in the Faradaic current[47,48] as observed in the region I/II in Figure 3a.

Regarding the energy storage capability of the resulting electrode material, the effect of V inclusion in the CoO$_x$ structure is better appreciated in Figure 3b. While the short plateau contribution at 0.15−0.2 V due to Co(OH)$_2$ → CoOOH conversion remains almost unchanged for all samples, the slope at E > 0.2 V shows evident differences, with the higher capacity values (lower slopes) displayed by sample S4 (300 F g^{-1}), followed by S3 (247 F g^{-1}) and S2 (180 F g^{-1}). The mean values of SC for the whole range (0−0.55 V) are summarized in Figure 4a.

In terms of SC, the best value was obtained in S4 sample; any further increase in V amounts results in a decrease in capacitance around 10% for S3, 23% for S2, and 64% for S1. This behavior suggests that a certain number of lattice defects, or distortion induced by V atoms, are necessary to facilitate the ion diffusion.[49] However, the distortion in the structure generated by the V atoms can influence the conductivity in the charge transfer (see Figure S5).

A comparison of the rate capability measured at current densities of 6, 4, 2, 1, and 0.5 A g^{-1} is presented in Figure 4b,c. The electrochemical performance shown in Figure 4b indicates that the capacitances of S3 and S4 samples at 6 A g^{-1} are remarkable, with values of 238 and 242 F g^{-1}, respectively. Both the rate capability and the specific capacity retention (Figure 4b,c) evidenced that oxides with lower amounts of V show the best performance, with values of 87 and 81% for S3 and S4 samples, respectively, and SC retention higher than 80%. As has been mentioned, in both cases, the high values of rate capability may be related to their crystal structure, which can permit exceptionally rapid ionic transport,[7] as well as a possible distortion in the crystal lattice caused by the variation in the size of the V ions in the form of V^{4+} (0.72 Å) and V^{3+} (0.78 Å).[50] It is also observed that through XPS analysis, the S4 sample showed large amounts of Co(OH)$_2$ and CoOOH

species in the structure (see Figure 2a), compared with S1 and S2 samples. The presence of $Co(OH)_2$ favors the diffusion process of OH^- ions within the material, which leads to improved electrochemical properties.[51] On the other hand, the low electrochemical performance of the samples that have a high content of vanadium (S2 and S1) could be due to the lack of electroactive sites of the conducting species of Co, generating a lower accessibility of the OH^- ions in the internal structure at high current densities, as shown in the work of Liu et al., who studied the influence of vanadium doping on birnessite, it was found that the charge-transfer resistance R_{ct} increased with an increase in doped vanadium content.[52] Furthermore, the addition of vanadium in the structure is reflected in the variety of oxidation states as shown in studies of $V_2O_5 \cdot nH_2O$[53] and is also evidenced in the Raman results in this work (see Figure 1b).

Another important result analyzed is the Coulombic efficiency (η) (Figure 4d). Although the Coulombic efficiency for most of the samples could be considered as high (>80%), for S4 sample, it was initially about 81% at a current density of 0.5 A g^{-1} and increases to nearly 93% when the current density is 6 A g^{-1}. This could be due to faster surface activation at high current density conditions and better electrochemical accessibility of OH^- ions to the surface compared with the other mentioned CoV oxides even at higher current density.[54,55] In addition, as expected for an electroactive material containing CoV oxide,[56] at low current densities and potential as high as 0.55 V, the parasitic side OER takes place,[40] which explains the lower Coulombic efficiency at 0.5 A g^{-1} for S4, indicating that this composition also presents prospects as an electrocatalyst for OER. On the other hand, at higher current densities, the contribution of OER parasitism is smaller, resulting in a Coulombic efficiency increase (Figure 4d).

A better understanding of the process that takes place at CoV oxides came from the analysis of the charge storage mechanism through the b parameter in Figure 5. The b-values as a function of electrode potential (V) for different CoV oxides are shown in Figure 5a. b-values well below 1 for the 0–0.15 V region are in good agreement with the occurrence of diffusion-controlled Faradic process $Co^{2+} \rightarrow Co^{3+}$ involving OH^- exchange. Once $Co(OH)_2$ conversion to CoOOH takes place ($E > 0.15$ V), the b-values sharply increase to 1, indicating that the surface double-layer charge is the main cause of the notorious increase in the current as observed for $E > 0.2$ V in Figure 3a. In Figure 5b, a typical b-value analysis is exemplified for $E = 0.125$ V. The obtained b-values at $E = 0.125$ V are 0.67, 0.53, 0.75, and 0.84 for S4, S3, S2, and S1, respectively. This result is consistent with those obtained by EIS, where the composition that has a greater amount of V atoms in the structure has a lower resistance to charge transfer R_{ct}. The R_{ct} values of 0.158, 1.86, 2.59, and 2.22 kΩ were achieved on the S1, S2, S3, and S4 surfaces, respectively (see Figure S5).

The selected potential corresponds to the onset for $Co(OH)_2$ conversion to CoOOH, and the b-values indicate that charge storage is due to a combination of surface- and diffusion-controlled processes. At slower scan rates, the SC is generated by the contribution of redox processes that occur in the internal structure, while at higher scanning rates, it limits the diffusion of electrolyte ions within the structure, and as a result, charge storage only depends on the outer surface of the electrode.[24]

Finally, Figure 6 resumes the partial surface capacitive contribution (first term in eq 6) to the total current, as a result of analysis using eqs 6 and (7). Results for all samples show that, at the low scan rate analyzed (1 mV s^{-1}), most contribution to the current at potentials more positive than peak I is due to surface-controlled processes (pseudocapacitive). As was previously observed in the analysis of Figure 5, at a potential below the $Co(OH)_2 \rightarrow$ CoOOH oxidation peak (I), a mixed behavior is observed, with a crescent contribution of the diffusion-controlled process as the potential is closer to the peak. This fact, however, is not so evident for the III/IV region previously assigned to the Co^{3+}/Co^{4+} couple, where most of the current contribution is due to pseudocapacitive contribution. In fact, for the V-free CoO_x sample (Figure S7), the pseudocapacitive current matches perfectly with the whole current between 0.2 and 0.5 V. In this potential window, conventional diffusion-controlled Faradaic reaction Co^{3+}/Co^{4+} (if exists) is negligible against surface-controlled processes.

Finally, even though the main part of the current can be attributed to the presence of V in the samples, the physicochemical nature of the process is even unsolved. Surface redox pseudocapacitance, as well as intercalation pseudocapacitance, may both exhibit identical i/v response. As stated above, the samples studied here were not calcined, so while the XRD patterns for all samples (Figure 1a) displayed a single phase of $Co_3V_2O_8$ with orthorhombic structure, Raman spectroscopy and XPS (Figures 1b and 2) show the existence of several, coexisting oxidation states for V, including V^{3+}, V^{4+}, and V^{5+} and the metastable formations of V_4O_9 at the surface. Even though the best behavior of the S4 sample suggests a synergic effect of Co–V with the lowest V load, reserving the role of the doping element for V, direct contributions of the vanadium redox states' interconversion at the CoV oxide surface cannot be discarded.

5. CONCLUSIONS

CoV oxides with different Co and V compositions were successfully synthesized by the solvothermal method using glycerol as a stabilizing agent. The XRD patterns obtained showed a crystalline structure corresponding to $Co_3V_2O_8$ with an orthorhombic structure in the absence of heat treatment. Raman spectroscopy and XPS showed the existence of several, coexisting oxidation states for V, including V^{3+}, V^{4+}, and V^{5+} and the metastable formations of V_4O_9 at the surface. Vanadium doping improved the performance of electrochemical capacitance due to the synergy of Co and V; with a minimum amount of V in the structure, it may distort the crystal lattice and improve the electrolyte diffusion, obtaining for the S4 sample a SC of up to 300 F g^{-1} at a current density of 0.5 A g^{-1}, with a capacitance retention of 81% evaluated from 0.5 to 6 A g^{-1}. The results presented in this study on the influence of the variation of the Co and V composition on CoV oxides exhibit electrochemical characteristics of a pseudocapacitive electrode material despite the fact that charge storage occurs in bulk. This behavior is consistent with the pseudocapacitance generated by redox processes, showing b values of 0.67, 0.53, 0.75, and 0.84, with a capacitive current contribution of 74, 74, 63, and 70% analyzed at a scan rate of 1 mV s^{-1} for S4, S3, S2, and S1 samples, respectively.

■ ASSOCIATED CONTENT

Ⓢⓘ Supporting Information

The Supporting Information is available free of charge at https://pubs.acs.org/doi/10.1021/acsomega.2c04126.

Physicochemical characterization of CoV oxides: TEM, SEM−EDS, XPS analysis, and electrochemical evaluation of CoV oxides at different scan rates and EIS spectroscopy analysis (PDF)

■ AUTHOR INFORMATION

Corresponding Author

Angélica Maria Baena-Moncada − *Laboratorio de Investigación de Electroquímica Aplicada, Facultad de Ciencias, Universidad Nacional de Ingeniería, Lima 15333, Peru;* ⊙ orcid.org/0000-0002-2896-4392; Phone: 0051955136208; Email: abaenam@uni.edu.pe

Authors

Lady V. Quispe-Garrido − *Laboratorio de Investigación de Electroquímica Aplicada, Facultad de Ciencias, Universidad Nacional de Ingeniería, Lima 15333, Peru*

Ivonne E. Monje − *Laboratorio de Investigación de Electroquímica Aplicada, Facultad de Ciencias, Universidad Nacional de Ingeniería, Lima 15333, Peru*

Elvis O. López − *Department of Experimental Low Energy Physics, Brazilian Center for Research in Physics (CBPF), Rio de Janeiro 22290-180, Brazil*

Josué M. Gonçalves − *Department of Fundamental Chemistry, Institute of Chemistry, University of São Paulo, São Paulo SP 05508-000, Brazil;* ⊙ orcid.org/0000-0003-0800-077X

Cleonice S. Martins − *Department of Experimental Low Energy Physics, Brazilian Center for Research in Physics (CBPF), Rio de Janeiro 22290-180, Brazil*

Gabriel Angel Planes − *Instituto de Investigación en Tecnologías Energéticas y Materiales Avanzados (IITEMA), CONICET, Universidad Nacional de Río Cuarto, Río Cuarto 5800 Córdoba, Argentina*

José G. Ruiz-Montoya − *Laboratorio de Investigación de Electroquímica Aplicada, Facultad de Ciencias, Universidad Nacional de Ingeniería, Lima 15333, Peru;* ⊙ orcid.org/0000-0001-9586-9152

Complete contact information is available at:
https://pubs.acs.org/10.1021/acsomega.2c04126

Notes

The authors declare no competing financial interest.

■ ACKNOWLEDGMENTS

■ REFERENCES

(1) Islam, M. S.; Fisher, C. A. Lithium and sodium battery cathode materials: Computational insights into voltage, diffusion and nanostructural properties. *Chem. Soc. Rev.* **2014**, *43*, 185−204.

(2) Dubey, P.; Shrivastav, V.; Maheshwari, P. H.; Sundriyal, S. Recent advances in biomass derived activated carbon electrodes for hybrid electrochemical capacitor applications: Challenges and opportunities. *Carbon* **2020**, *170*, 1−29.

(3) Choi, C.; Ashby, D. S.; Butts, D. M.; DeBlock, R. H.; Wei, Q.; Lau, J.; Dunn, B. Achieving high energy density and high power density with pseudocapacitive materials. *Nat. Rev. Mater.* **2020**, *5*, 5−19.

(4) Simon, P.; Gogotsi, Y. Perspectives for electrochemical capacitors and related devices. *Nat. Mater.* **2020**, *19*, 1151−1163.

(5) Zhao, X.; Sánchez, B. M.; Dobson, P. J.; Grant, P. S. The role of nanomaterials in redox-based supercapacitors for next generation energy storage devices. *Nanoscale* **2011**, *3*, 839−855.

(6) Simon, P.; Gogotsi, Y. Materials for electrochemical capacitors. *Nat. Mater.* **2008**, *7*, 845−854.

(7) Augustyn, V.; Come, J.; Lowe, M. A.; Kim, J. W.; Taberna, P.-L.; Tolbert, S. H.; Abruña, H. D.; Simon, P.; Dunn, B. High-rate electrochemical energy storage through Li+ intercalation pseudocapacitance. *Nat. Mater.* **2013**, *12*, 518−522.

(8) Brousse, T.; Bélanger, D.; Long, J. W. To Be or Not To Be Pseudocapacitive? *J. Electrochem. Soc.* **2015**, *162*, A5185−A5189.

(9) Cottineau, T.; Toupin, M.; Delahaye, T.; Brousse, T.; Bélanger, D. Nanostructured transition metal oxides for aqueous hybrid electrochemical supercapacitors. *Appl. Phys. A: Mater. Sci. Process.* **2006**, *82*, 599−606.

(10) Li, X.; Jiang, L.; Zhou, C.; Liu, J.; Zeng, H. Integrating large specific surface area and high conductivity in hydrogenated NiCo2O4 double-shell hollow spheres to improve supercapacitors. *NPG Asia Mater.* **2015**, *7*, No. e165.

(11) Lim, P. T.; Azman, N. H. N.; Kulandaivalu, S.; Sulaiman, Y. Three-dimensional network of poly(3,4-ethylenedioxythiophene)/nanocrystalline cellulose/cobalt oxide for supercapacitor. *Polymer* **2022**, *250*, 124888.

(12) Balaji, T. E.; Tanaya Das, H.; Maiyalagan, T. Recent trends in bimetallic oxides and their composites as electrode materials for supercapacitor applications. *ChemElectroChem* **2021**, *8*, 1723−1746.

(13) Li, Q.; Zhang, Q.; Zhou, Z.; Gong, W.; Liu, C.; Feng, Y.; Hong, G.; Yao, Y. Boosting Zn-ion storage capability of self-standing Zn-doped Co3O4 nanowire array as advanced cathodes for high-performance wearable aqueous rechargeable Co//Zn batteries. *Nano Res.* **2021**, *14*, 91−99.

(14) Gonçalves, J. M.; da Silva, M. I.; Toma, H. E.; Angnes, L.; Martins, P. R.; Araki, K. Trimetallic oxides/hydroxides as hybrid supercapacitor electrode materials: a review. *J. Mater. Chem. A* **2020**, *8*, 10534−10570.

(15) Li, Q. Interfacial Control of NiCoP@NiCoP Core-Shell Nanoflake Arrays as Advanced Cathodes for Ultrahigh-Energy-Density Fiber-Shaped Asymmetric Supercapacitors. *Small* **2021**, *17*, 2101617.

(16) Li, Q.; Zhang, Q.; Sun, J.; Liu, C.; Guo, J.; He, B.; Zhou, Z.; Man, P.; Li, C.; Xie, L.; Yao, Y. All Hierarchical Core-Shell Heterostructures as Novel Binder-Free Electrode Materials for Ultrahigh-Energy-Density Wearable Asymmetric Supercapacitors. *Adv. Sci.* **2019**, *6*, 1801379.

(17) Li, Q.; Jing, S.; Yong, Z.; Zhang, Q.; Liu, C.; Zhu, K.; Feng, Y.; Gong, W.; Yao, Y. Towards ultrahigh-energy-density flexible aqueous rechargeable Ni//Bi batteries: Free-standing hierarchical nanowire arrays core-shell heterostructures system. *Energy Storage Mater.* **2021**, *42*, 815−825.

(18) Zhang, Y.; Liu, Y.; Chen, J.; Guo, Q.; Wang, T.; Pang, H. Cobalt vanadium oxide thin nanoplates: primary electrochemical capacitor application. *Sci. Rep.* **2014**, *4*, 5687.

(19) Wu, F.; Xiong, S.; Qian, Y.; Yu, S.-H. Hydrothermal Synthesis of Unique Hollow Hexagonal Prismatic Pencils of Co3V2O8·n H2O:

A New Anode Material for Lithium-Ion Batteries. *Angew. Chem.* **2015**, *127*, 10937−10941.

(20) Zhang, J.; Yuan, B.; Cui, S.; Zhang, N.; Wei, J.; Wang, X.; Zhang, D.; Zhang, R.; Huo, O. Facile synthesis of 3D porous Co3V2O8 nanoroses and 2D NiCo2V2O8 nanoplates for high performance supercapacitors and their electrocatalytic oxygen evolution reaction properties. *Dalton Trans.* **2017**, *46*, 3295−3302.

(21) Sun, H.; Chen, X.; Chai, H.; Wang, Y.; Jia, D.; Cao, Y.; Liu, A. 3D porous hydrated cobalt pyrovanadate microflowers with excellent cycling stability as cathode materials for asymmetric supercapacitor. *Appl. Surf. Sci.* **2019**, *469*, 118−124.

(22) Teng, Y.; Li, Y.; Yu, D.; Meng, Y.; Wu, Y.; Zhao, X.; Liu, X. The Microwave-Assisted Hydrothermal Synthesis of CoV2 O6 and Co3 V2 O8 with Morphology Tuning by pH Adjustments for Super-capacitor Applications. *ChemistrySelect* **2019**, *4*, 956−962.

(23) Liu, M. C.; Kong, L. B.; Kang, L.; Li, X.; Walsh, F. C.; Xing, M.; Lu, C.; Ma, X.-J.; Luo, Y.-C. Synthesis and characterization of M3V2O8 (M = Ni or Co) based nanostructures: A new family of high performance pseudocapacitive materials. *J. Mater. Chem. A* **2014**, *2*, 4919−4926.

(24) Ray, A.; Roy, A.; Saha, S.; Ghosh, M.; Roy Chowdhury, S.; Maiyalagan, T.; Bhattacharya, S. K.; Das, S. Electrochemical energy storage properties of Ni-Mn-oxide electrodes for advance asymmetric supercapacitor application. *Langmuir* **2019**, *35*, 8257−8267.

(25) Sauerbrei, E. E.; Faggiani, R.; Calvo, C. Refinement of the crystal structure of Co3V2O8 and Ni3V2O8. *Acta Crystallogr., Sect. B: Struct. Crystallogr. Cryst. Chem.* **1973**, *29*, 2304−2306.

(26) Cullity, B. D. *Elements of X-ray Diffraction*, 2nd ed.; Addison-Wesley Publishing Company, 1978.

(27) Low, W. H.; Siong, C. W.; Chia, C. H.; Lim, S. S.; Khiew, P. S. A facile synthesis of graphene/Co3V2O8 nanocomposites and their enhanced charge storage performance in electrochemical capacitors. *J. Sci.: Adv. Mater. Devices* **2019**, *4*, 515−523.

(28) Lee, S.-H.; Cheong, H. M.; Seong, M. J.; Liu, P.; Tracy, C. E.; Mascarenhas, A.; Pitts, J. R.; Deb, S. K. Raman spectroscopic studies of amorphous vanadium oxide thin films. *Solid State Ionics* **2003**, *165*, 111−116.

(29) Malkov, A. A.; Malygin, A. A. Synthesis and thermochemical transformations of vanadium oxychloride groups on a silica surface. *Russ. J. Phys. Chem. A* **2014**, *88*, 530−536.

(30) Shvets, P.; Dikaya, O.; Maksimova, K.; Goikhman, A. A review of Raman spectroscopy of vanadium oxides. *J. Raman Spectrosc.* **2019**, *50*, 1226−1244.

(31) Miyake, T.; Doi, T. Importance of a quasistable V4O9 to synthesize a highly crystalline VOHPO4·0.5H2O. *Appl. Catal., A* **1995**, *131*, 43−54.

(32) Biesinger, M. C.; Lau, L. W. M.; Gerson, A. R.; Smart, R. S. C. Resolving surface chemical states in XPS analysis of first row transition metals, oxides and hydroxides: Sc, Ti, V, Cu and Zn. *Appl. Surf. Sci.* **2010**, *257*, 887−898.

(33) Moulder, J. F.; Chastain, J.; King, R. *Handbook of X-Ray Photoelectron Spectroscopy: A Reference Book of Standard Spectra for Identification and Interpretation of XPS Data*; Eden Prair. Perkin-Elmer Corp., 1995.

(34) Wang, R.; Yan, X. Superior asymmetric supercapacitor based on Ni-Co oxide nanosheets and carbon nanorods. *Sci. Rep.* **2014**, *4*, 3712.

(35) Horvath, B.; Strutz, J.; Geyer-Lippmann, J.; Horvath, E. G. Preparation, Properties, and ESCA Characterization of Vanadium Surface Compounds on Silicagel. I. ZAAC. *J. Inorg. Gen. Chem.* **1981**, *483*, 181−192.

(36) Akiba, K.; Matsubayashi, G. Spectroscopy and electrical properties of oxidized tris(dmit)vanadium anion complex (dmit=4,5-dimercapto-1,3-dithiole-2-thionate). *Inorg. Chim. Acta.* **1989**, *165*, 245−248.

(37) Biesinger, M. C.; Payne, B. P.; Grosvenor, A. P.; Lau, L. W. M.; Gerson, A. R.; Smart, R. S. C. Resolving surface chemical states in XPS analysis of first row transition metals, oxides and hydroxides: Cr, Mn, Fe, Co and Ni. *Appl. Surf. Sci.* **2011**, *257*, 2717−2730.

(38) Nag, N. K.; Massoth, F. E. ESCA and gravimetric reduction studies on V/Al2O3 and V/SiO2 catalysts. *J. Catal.* **1990**, *124*, 127−132.

(39) Lv, X.; huang, W.; Shi, Q.; Tang, L.; Tang, J. Synthesis of CoV2O6/CNTs composites via ultrasound as electrode materials for supercapacitors. *J. Mater. Sci. Mater. Electron.* **2020**, *31*, 2388−2397.

(40) Gonçalves, J. M.; Martins, P. R.; Araki, K.; Angnes, L. Recent progress in water splitting and hybrid supercapacitors based on nickel-vanadium layered double hydroxides. *J. Energy Chem.* **2021**, *57*, 496−515.

(41) Wang, J.; Polleux, J.; Lim, J.; Dunn, B. Pseudocapacitive contributions to electrochemical energy storage in TiO2 (anatase) nanoparticles. *J. Phys. Chem. C* **2007**, *111*, 14925−14931.

(42) Fernando, J. F. S.; Siriwardena, D. P.; Firestein, K. L.; Zhang, C.; von Treifeldt, J. E.; Lewis, C.-E. M.; Wang, T.; Dubal, D. P.; Golberg, D. V. Enriched pseudocapacitive lithium storage in electrochemically activated carbonaceous vanadium(iv, v) oxide hydrate. *J. Mater. Chem. A* **2020**, *8*, 13183−13196.

(43) Gonçalves, J. M.; da Silva, M. I.; Silva, M. N. T.; Martins, P. R.; Nossol, E.; Toma, H. E.; Angnes, L. Recent progress in ZnCo2O4 and their composites for energy storage and conversion: A review. *Energy Adv.* **2022**, *1*, 793.

(44) Lang, J. W.; Kong, L. B.; Wu, W. J.; Luo, Y. C.; Kang, L. Facile approach to prepare loose-packed NiO nano-flakes materials for supercapacitors. *Chem. Commun.* **2008**, 4213−4215.

(45) Conway, B. E. Transition from "supercapacitor" to "battery" behavior in electrochemical energy storage. *Proceedings of the International Power Sources Symposium*; Publ by IEEE, 1991; Vol. *138*, pp 319−327.

(46) Wu, Z.; Khalafallah, D.; Teng, C.; Wang, X.; Zou, Q.; Chen, J.; Zhi, M.; Hong, Z. Vanadium doped hierarchical porous nickel-cobalt layered double hydroxides nanosheet arrays for high-performance supercapacitor. *J. Alloys Compd.* **2020**, *838*, 155604.

(47) Huang, B.; Wang, W.; Pu, T.; Li, J.; Zhao, C.; Xie, L.; Chen, Yu. Rational design and facile synthesis of two-dimensional hierarchical porous M3V2O8 (M = Co, Ni and Co-Ni) thin sheets assembled by ultrathin nanosheets as positive electrode materials for high-performance hybrid supercapacitors. *Chem. Eng. J.* **2019**, *375*, 121969.

(48) Li, M.; Ma, K. Y.; Cheng, J. P.; Lv, D.; Zhang, X. B. Nickel-cobalt hydroxide nanoflakes conformal coating on carbon nanotubes as a supercapacitive material with high-rate capability. *J. Power Sources* **2015**, *286*, 438−444.

(49) Naveen, A. N.; Selladurai, S. Investigation on physiochemical properties of Mn substituted spinel cobalt oxide for supercapacitor applications. *Electrochim. Acta* **2014**, *125*, 404−414.

(50) Park, H. W.; Na, B.-K.; Cho, B. W.; Park, S.-M.; Roh, K. C. Influence of vanadium doping on the electrochemical performance of nickel oxide in supercapacitors. *Phys. Chem. Chem. Phys.* **2013**, *15*, 17626−17635.

(51) Yu, Y.; Wang, H.; Zhang, H.; Tan, Y.; Wang, Y.; Song, K.; Yang, B.; Yuan, L.; Shen, X.; Hu, X. Blanket-like Co(OH)2/CoOOH/Co3O4/Cu(OH)2 composites on Cu foam for hybrid supercapacitor. *Electrochim. Acta* **2020**, *334*, 135559.

(52) Liu, L.; Min, M.; Liu, F.; Yin, H.; Zhang, Y.; Qiu, G. Influence of vanadium doping on the supercapacitance performance of hexagonal birnessite. *J. Power Sources* **2015**, *277*, 26−35.

(53) Lee, H. Y.; Goodenough, J. B. Ideal Supercapacitor Behavior of Amorphous V2O5·nH2O in Potassium Chloride (KCl) Aqueous Solution. *J. Solid State Chem.* **1999**, *148*, 81−84.

(54) Meher, S. K.; Rao, G. R. Enhanced activity of microwave synthesized hierarchical MnO2 for high performance supercapacitor applications. *J. Power Sources* **2012**, *215*, 317−328.

(55) Meher, S. K.; Justin, P.; Ranga Rao, G. Microwave-mediated synthesis for improved morphology and pseudocapacitance perform-ance of nickel oxide. *ACS Appl. Mater. Interfaces* **2011**, *3*, 2063−2073.

(56) Gonçalves, J. M.; da Silva, M. I.; Angnes, L.; Araki, K. Vanadium-containing electro and photocatalysts for the oxygen evolution reaction: a review. *J. Mater. Chem. A* **2020**, *8*, 2171−21206.